Supporting Information

Ensemble Effects in Cu/Au Ultrasmall Nanoparticles Control the Branching Point for C1 Selectivity During CO_2 Electroreduction

Hongyu Shang,[a] Dongjoon Kim,[b] Spencer K. Wallentine,[a] Minkyu Kim,[c] Daniel M. Hofmann,[d] Runiya Dasgupta,[a] Catherine J. Murphy,*[d] Aravind Asthagiri,*[b] L. Robert Baker*[a]

a. Department of Chemistry and Biochemistry, The Ohio State University, 100 W. 18th Ave., Columbus, OH 43210. Email: baker.2364@osu.edu
b. Department of Chemical and Biomolecular Engineering, The Ohio State University, 151 W. Woodruff Ave., Columbus, OH 43210. Email: asthagiri.1@osu.edu
c. School of Chemical Engineering, Yeungnam University, 280 Daehak-Ro, Gyeongsan 38541, Republic of Korea
d. Department of Chemistry, University of Illinois at Urbana-Champaign, 600 S. Matthews Ave., Urbana, IL 61801. Email: murphycj@illinois.edu

Table of Contents

S1. Experimental details

Sample preparation

All chemicals were purchased from Sigma Aldrich and were used without further purification. The synthesis of the nanoparticles used in this study was reported previously.[1] Here we provide a brief summary of the modified Brust method. A 40 mL solution of 50 mM tetraoctylammonium bromide (TOAB) in toluene was added to a round bottom flask. Hydrogen tetrachloroaurate trihydrate ($HAuCl_4 \cdot 3H_2O$, 99.9%) and copper(II) chloride dihydrate ($CuCl_2 \cdot 2H_2O$, 99.9%) were used as metal salt precursors for gold and copper, respectively. The appropriate ratio of these salts were mixed to form a solution with total metal ion concentration of 30 mM in excess KCl, and 15 mL of this precursor solution was added to the TOAB solution. Next 0.12 mL of neat dodecanethiol was added followed by the dropwise addition of 12.5 mL of 0.4 M $NaBH_4$, and the solution was stirred for 3 h. The organic phase containing the nanoparticles was then separated from the aqueous phase followed by precipitation in ethanol. Following two additional wash cycles in ethanol, the particles were dried under vacuum and redispersed in toluene.

The working electrode was produced by polishing glassy carbon with 50 nm alumina polish followed by washing with Milli-Q water and drying in nitrogen. The nanoparticles were then dropcast to give the mass loadings, given in Table S1. These mass loadings were chosen to give similar particle densities when accounting for atomic mass.

Table S1. Nanoparticle mass loading by composition.

Composition	Mass per sample (mg)
Au	0.25
3Au1Cu	0.22
1Au1Cu	0.19
1Au3Cu	0.16
Cu	0.11

Electrochemical measurements

Electrochemical measurements were performed in a custom glass H-Cell using a Biologic SP-50 potentiostat/galvanostat. The working electrode and reference electrode (Low Profile Ag/AgCl) were separated from the counter electrode (Pt film) by a nafion membrane. Prior to each measurement the nafion membrane was activated in 10% H_2SO_4 at 80 °C for 10 minutes.

The H-cell was equipped with a gas tight cap, through which gases were pumped to a gas chromatograph (Agilent 7890 B). Gas products were separated using a molecular sieve column and quantified using a thermal conductivity detector (Hydrogen) and a nickel catalyst with subsequent flame ionization detector (CO). Prior to experiments, the headspace was filled with high purity CO_2 (Praxair, 99.9%) to atmospheric pressure, and the 0.1 M sodium bicarbonate (Sigma-Aldrich 99.5% in milli-Q water 18.2 Ohm) electrolyte was purged until the pH reached 6.8. During experiments, the CO_2 saturated headspace was continually bubbled through the electrolyte.

Faradaic selectivity calculations

Due to incomplete mixing of headspace gases, the gas phase products do not sum to 100% Faradaic efficiency as is well known. To compensate for this, the Faradaic efficiency of H_2 and CO was normalized, such that the total Faradaic efficiency was 100% consistent with previous reports.[2,3] To do this, a normalization factor is calculated for the gas products at each composition under different potentials, and a standard deviation for this normalization factor across all measurements is obtained. Error bars for CO and H_2 Faradaic selectivity represent uncertainty for each measurement based on the standard deviation of the normalization factor. To determine uncertainty in the Faradaic efficiency to HCOOH, a linear regression[4] was performed based on the measurement of HCOOH standards prepared at different concentrations and calibrated by NMR in the presence of an internal standard. Error bars for HCOOH Faradaic selectivity represent uncertainty for each measurement based on the standard deviation of the absolute HCOOH concentration determined from this linear regression.

S2. Catalyst cyclic voltammograms and deactivation profiles

Figure S1 shows cyclic voltammetry measurements for each bimetallic nanoparticle composition in CO_2 and Argon purged electrolyte. Au nanoparticles show the highest current density and Cu nanoparticles show the lowest current density in both cases. The total current as a function of time during electrolysis and under the most reducing potential –1.1 V vs. RHE is shown in Figure S2. The total current is stable during the experiment. Similar stable currents were also detected under all other potentials.

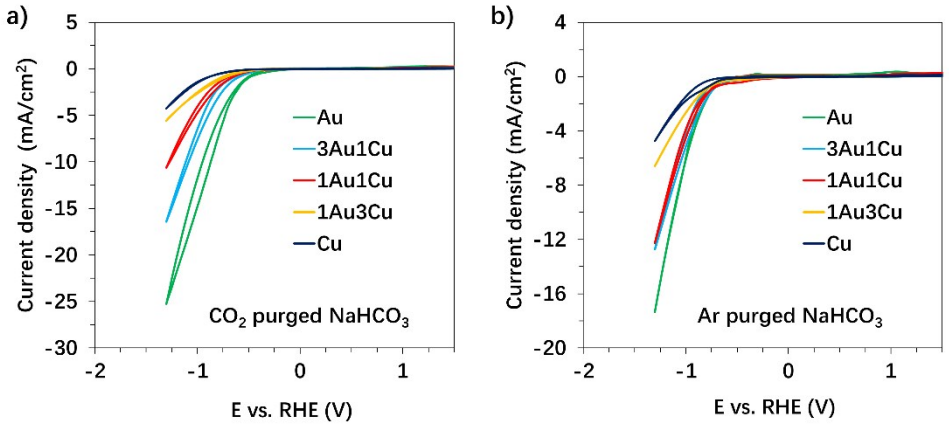

Figure S1. Cyclic Voltammetry of bimetallic nanoparticles in 0.1M $NaHCO_3$ saturated with (a) CO_2 and (b) Ar. Current density is normalized by ECSA. Scan rate 20 mV/sec.

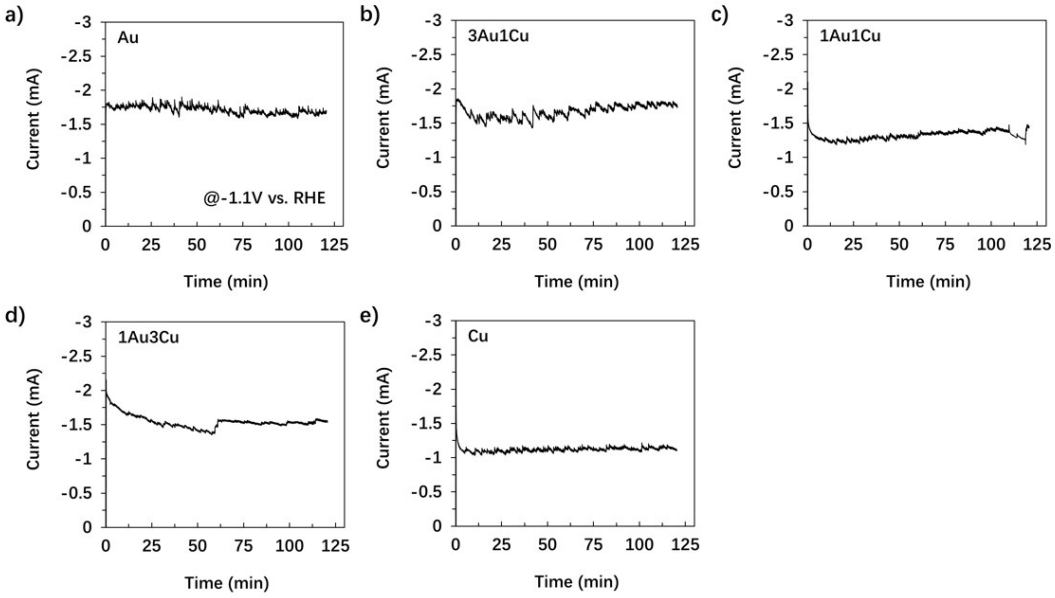

Figure S2. Total current as a function of time for different compositions under –1.1 V vs. RHE.

S3. Pre-reaction and post-reaction TEM

To confirm the stability of the nanoparticles during reaction we collect post reaction TEM images of the Au nanoparticles after 120 minutes at the most reducing potential, -1.1 V vs. RHE. The particles were dissolved off the electrode in chloroform and imaged. An HAADF-STEM image of the pre-reaction particles is provided in Figure S3a and the corresponding size histogram is shown below in Figure S3b. A TEM image and corresponding size histogram of the post-reaction particles are shown below in Figure S3c and 3d. Comparison of the histograms shows that the post-reaction particles have a size distribution within error of the pre-reaction particles. The HAADF-STEM image in Figure S3a was collected by a Thermo Scientific Themis Z S/TEM at 300kV. The TEM image in Figure S1c was collected by a JEOL 2010F transmission electron microscope/scanning transmission electron microscope. Similar TEM results are shown for 3Au1Cu in Figure S4. After removal of the ligand by UV ozone, the 3Au:1Cu nanoparticles grow larger in size by about 30%.

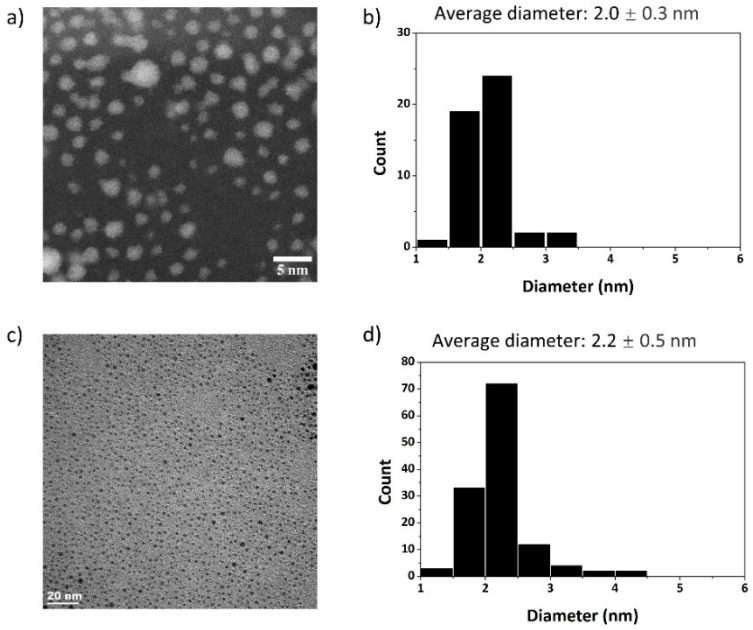

Figure S3. (a) High-angle annular dark-field scanning transmission electron micrograph (HAADF-STEM) and (b) corresponding histogram of fresh Au nanoparticles. (c) TEM image and (d) corresponding histogram of 2-hour post electrolysis Au nanoparticles.

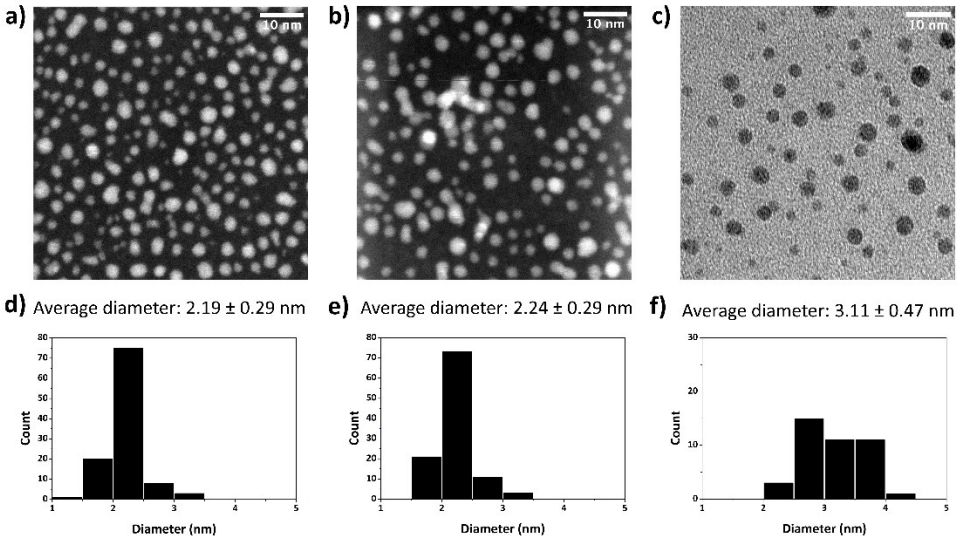

Figure S4. (a, b, c) TEM image and (d, e, f) corresponding histogram of pre- and post-reaction 3Au1Cu nanoparticles and UVO 3Au1Cu nanoparticles.

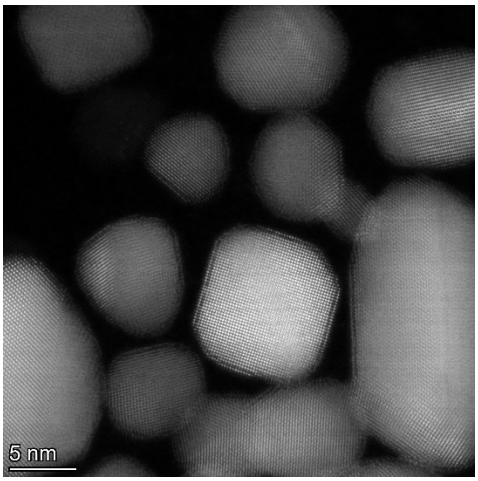

Figure S5. HAADF-STEM image of a 1Au:1Cu particle after heating at 200 C in vacuum to remove the dodecanethiol ligand.

Figure S5 shows an HAADF-STEM image of the 1Au:1Cu nanoparticles after heating at 200 C in vacuum to remove the ligand. The particles grow significantly is size and also show evidence of a Au surface structure with a Cu underlayer and a bimetallic core.

S4. Catalyst electrochemical active surface areas and turnover frequencies

Electrochemical active surface area (ECSA) measurements were performed for each catalyst in order to obtain a surface site density for turn over frequency (TOF) calculations. These measurements are obtained by measuring the ferricyanide/ferrocyanide redox couple at different scan rates, and assumes that this couple is site independent. These associated plots allow us to obtain the peak current I_p.

$$I_p = (2.69 \times 10^5)\, n^{3/2} A D^{1/2} C v^{1/2}$$

Where n is the number of electrons transferred, A is the ECSA (cm^2), D is the diffusion coefficient (cm^2/s), C is the concentration of potassium ferrocyanide (mol/cm^3), and v is the scan rate (V/s). The diffusion rate is given by Konopka et al.[5] and D_O(ferri-)Fe^{3+} = 0.726 (+/-0.011) x 10^{-5}, D_R(ferrocyanide)Fe^{2+} = 0.667 (+/-0.014) x 10^{-5}, n is 1 for this redox couple, C is 5 mM, and the scan rates were 10, 20, 50, 100mV/s. In principle one can obtain the ECSA with one measurement; however a more precise measurement can be made by fitting a line to a plot of I_p vs $v^{1/2}$, where division of the slope by the other constants yields the ECSA as was performed here. Table S2 gives the resulting ECSA for each sample:

Table S2: Electrochemically active surface areas measured using the ferricyanide/ferrocyanide redox couple.

Composition	ECSA (cm^2)
Au	0.15
3Au1Cu	0.20
1Au1Cu	0.23
1Au3Cu	0.49
Cu	0.37

The main products of CO_2R were CO, H_2 (from water), and $HCOO^-$ (or HCOOH depending on pH). The additional gas products methane and ethylene are also detectable but with a FE of less than 0.5% and are not included in the table below. The liquid product $HCOO^-$, was detected by ^{1}H-Nuclear Magnetic Resonance (NMR). The turnover frequency (TOF) for each of the main products are listed in table S3. Turn over frequency was calculated using the lattice spacing of 0.235 nm for Au observed in the HAADF-STEM images, and assumes a (111) surface for simplicity. The measured lattice spacing of 0.20 nm was used for Cu.[6] The lattice spacing for the bimetallic nanoparticles was calculated using Vegard's law. The site densities are on the order of 2-3x10^{15} sites/cm^2. The reported TOF is an average over all sites, however carbon dioxide reduction is known to occur at undercoordinated sites[7–10], so the actual TOF at the most active sites may be higher. The reported TOF are on the same order as have been reported previously.[11]

Table S3. TOF and Mass activity of each product as a function of potential.

-0.9 V vs. RHE	CO TOF (s^{-1})	H_2 TOF (s^{-1})	HCOOH TOF (s^{-1})
Au	6.2	2.7	0
3Au1Cu	2.0	3.7	0.90
1Au1Cu	1.2	3.1	0.42
1Au3Cu	1.2	1.9	0
Cu	0.070	3.3	0

-1 V vs. RHE	CO TOF (s^{-1})	H_2 TOF (s^{-1})	HCOOH TOF (s^{-1})
Au	11	3.5	0
3Au1Cu	2.4	7.7	0.76
1Au1Cu	0.84	4.1	0.25
1Au3Cu	1.7	6.7	0
Cu	0.19	3.9	0.02

-1.1 V vs. RHE	CO TOF (s^{-1})	H_2 TOF (s^{-1})	HCOOH TOF (s^{-1})
Au	14	3.2	0
3Au1Cu	3.0	9.2	1.0
1Au1Cu	2.0	6.2	0.19
1Au3Cu	2.0	7.4	0
Cu	0.78	5.8	0

S5. Pre-reaction and post-reaction XPS of the Au and 3Au:1Cu

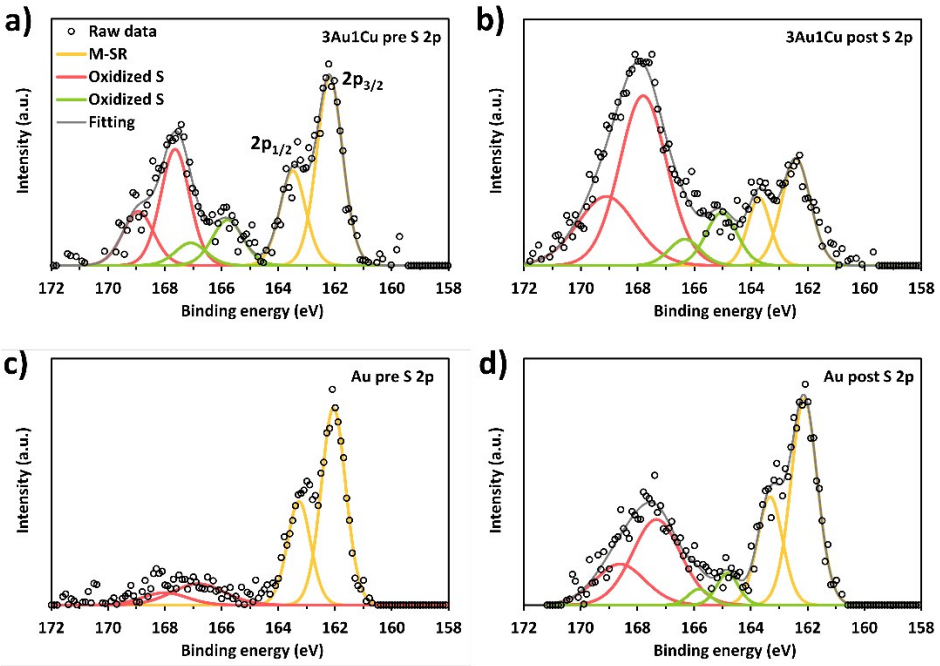

Figure S6. S 2p edge of pre- and post-reaction XPS of the Au and 3Au1Cu nanoparticles.

XPS at the S 2p edge of pre- and post-reaction 3Au:1Cu and Au nanoparticles are shown in figure S6 a, b and c, d respectively. All spectra show the same three spin orbit pairs except the pre-reaction Au which is missing the intermediate species. The lower energy S species at ~162 and 163 eV are from ligand (Metal-Sulfur-R). The other spin orbit pairs represent more oxidized S.[12–14] Post-reaction XPS shows a higher fraction of oxidized sulfur species. Both Au and 3Au:1Cu show the same S species, however Au shows no selectivity to HCOOH while 3Au:1Au shows the highest HCOOH selectivity, suggesting that the ligand has a negligible effect on the catalysis. We have previously made measurements on these systems and have shown that the ligand is stable during 2 hr. electrokinetic experiments.[15]

S6. Ensemble distribution calculation

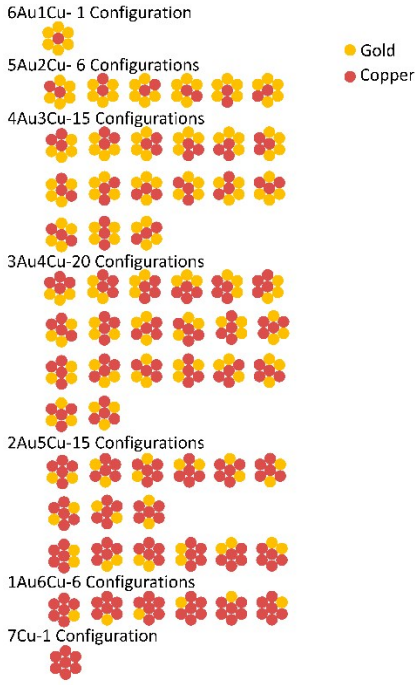

Figure S7. Possible ensemble configurations assuming a copper exists on the surface. (Red-Copper, Yellow-Gold)

To determine the ensemble probability distribution shown in Figure 5 of the main manuscript we considered a simple close-packing structure. Assuming a copper atom exists on the surface we consider the unique ensembles produced as different neighboring copper atoms are added. There are sixty-four unique combinations of neighboring atoms that fill the close-packing structure with up to seven copper atoms. We have considered all sixty four of these combinations and determined the contributions of each copper atom to Cu_1, Cu_2, or Cu_3 to each ensemble. All sixty-four ensembles are shown in Figure S7. The ensemble probability distributions were calculated as follows:

For each of the 64 configurations we sum the number of Cu atoms that contribute to:

1. Cu_1 sites (i.e. Cu atom with only nearest neighbor Au atoms)
2. Cu_2 sites (i.e. 2 adjacent Cu atoms not part a Cu_3 site)
3. Cu_3 sites (i.e. 3 Cu atoms each coordinating the other 2)

By this definition Cu_3 sites are those which form a 3-fold hollow between 3 adjacent Cu atoms, and Cu_2 sites are those which form only bridging sites between 2 adjacent Cu atoms. Note that in certain configurations, some Cu atoms are part of both a Cu_2 and Cu_3 site (e.g. the central atom in the 2nd and 3rd rows of the 3Au4Cu configurations shown above). In this case the central atom in question is fractionally proportioned between the multiple sites (e.g. counted as a half atom contribution to a Cu_2 and Cu_3 ensemble).

The number of Cu_n sites (n=1, 2, or 3) in each configuration is determined by taking the number of contributing Cu atoms divided by n. This normalization by n reflects that it requires 3 Cu atoms to compose one Cu_3 site and 2 Cu atoms to compose one Cu_2 site.

The number of Cu_n sites are then weighted by the composition-dependent probability for each of the 64 configurations and summed to produce a composition dependent probability distribution of Cu_1, Cu_2, and Cu_3 sites.

The resulting distribution is plotted in Figure 5 of the main manuscript. As expected, this distribution shows that Cu_1 sites are most prevalent at low Cu concentration. Cu_2 sites peak at approximately 25% Cu, and at high Cu composition Cu_3 sites become dominant.

S7. Computational details

All plane wave DFT calculations were performed using the projector augmented wave pseudopotentials[16] provided in the Vienna ab initio simulation package (VASP).[17,18] The Perdew-Burke-Ernzerhof (PBE) exchange-correlation functional[19] was used with a plane wave expansion cutoff of 400 eV. We use (211) slabs to represent the most relevant sites on the metal nanoparticles. The PBE bulk lattice constants of Au and Cu (4.08 Å (Au) and 3.64 Å (Cu)) are used to fix the lateral dimensions of the pure Au(211) and Cu(211) slab, respectively, and the corresponding surfaces are shown in Figure S8. The results in the manuscript (Figure 3) use Cu doping of pure Au(211) and the pure Cu(211) slab, but other configurations incorporating bimetallic alloy sublayers are discussed in Section S9 below. The surfaces are made of 4 layers (where a layer is defined by the surface exposed atoms and is illustrated by solid lines in the side view shown in Figure S8 b) resulting in ~9.1 Å thick slabs. The two bottom layers are fixed and a vacuum spacing of ~ 20 Å was included. This vacuum is sufficient to reduce the periodic interaction in the surface normal direction. Atoms in the top 2 layers are allowed to relax during the calculations until the forces are less than 0.03 eV/Å. In terms of system size, a 2×3 unit cell with a corresponding $2 \times 2 \times 1$ Monkhorst-Pack k-point mesh is employed for the (211) slabs. Unless otherwise noted, our DFT calculations were performed for a single molecule adsorbed within the 2×3 (211) surfaces.

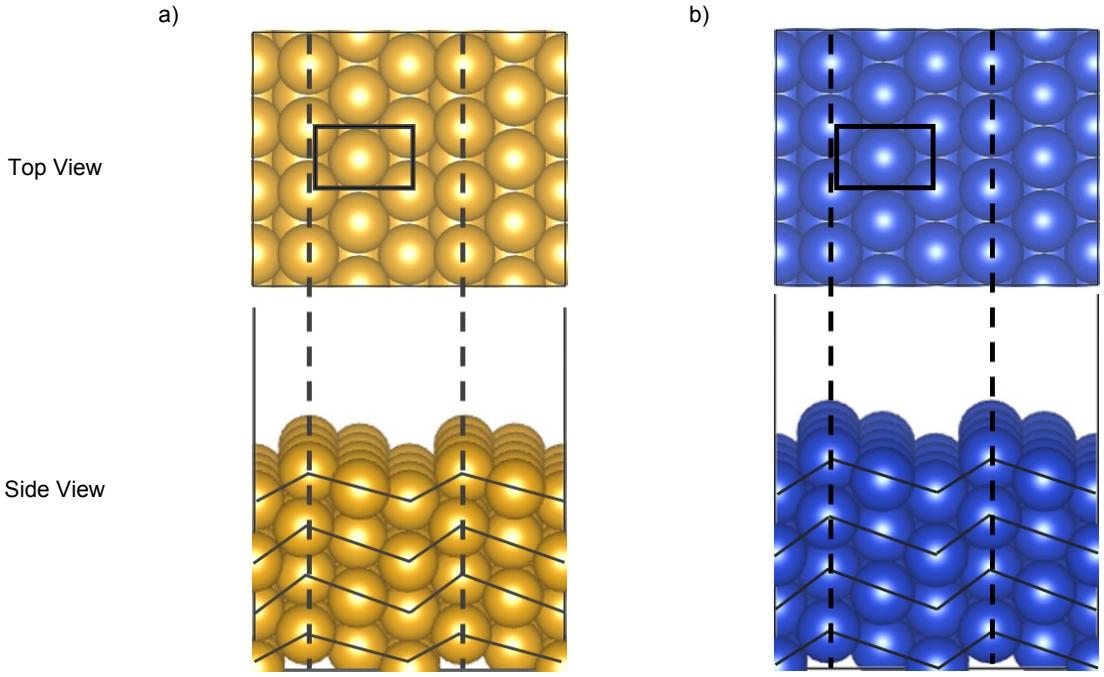

Figure S8. Illustration of top and side views of (a) Au(211), (b) Cu(211). The black box shown in top view indicates a 1×1 unit cell of the (211) surface and we use a 2×3 surface cell for the calculations. The dashed lines illustrate the step edge of the (211) surface and the solid lines in the side view illustrate the layers with the top layer consisting of the surface atoms. Yellow and blue atoms are Au and Cu, respectively.

In the present study, we evaluate the potential dependent reaction free energy (ΔG) for a coupled proton-electron elementary reaction by using the computational hydrogen electrode (CHE) model.[20] The ΔG of $A^* + H^+ + e^- \leftrightarrow AH^*$ can be described by

$$\Delta G = G(AH^*) - G(A^*) - \left[G(H^+) + G(e^-)\right] \#(1)$$

where * indicates an adsorbed molecule on the surface. In the CHE method we use the equivalence of free energy of the proton-electron pair and a hydrogen molecule in the standard state at 0 V of the reference hydrogen electrode (RHE) potential. The energy of the electron is assumed to be linearly dependent on the applied potential. The $\left[G(H^+) + G(e^-)\right]$ can be re-written as $\left[\frac{1}{2}G(H_2) - eU\right]$ based on the arguments above. After replacing the $\left[G(H^+) + G(e^-)\right]$ with the potential dependent term of $\left[\frac{1}{2}G(H_2) - eU\right]$, the potential dependency of free energy is determined linearly by shifting the electron energy − eU, where e is the elementary positive charge and U is the applied electrode potential on the RHE scale. We use DFT calculations combining with partition functions based on statistical mechanics to evaluate the free energies in the above equations. The free energy for H_2O(aq), HCOOH(aq), and CO_2(aq) are adjusted from the ideal gas phase DFT free energies assuming a fugacity of 3534 Pa, 2 Pa, and 101325 Pa, respectively.[21] To approximate solvation corrections, we have employed corrections that R-OH* (COOH*) and CO* are stabilized by 0.25 eV and 0.1 eV, respectively.[21] This approach approximately takes into account the additional stabilization through hydrogen bonding of COOH* versus CHOO* due to the water bilayer.

S8. Cu-Cu surface dopant interactions

We tested preference of surface dopant configurations by introducing 2 Cu surface dopants on Au (111) and Au(211) surfaces. Figure S9 shows top views of Cu surface dopant sites on Au(111) and Au(211). We compared the DFT surface energies of 4 different paired Cu surface dopant cases (Case1: site 1 – site 2, Case2: site 1 – site 3, Case3: site 1 – site 4 , Case4: site 1 – site 5). Table S4 shows the resulting relative DFT energies for the various Cu pair cases on Au(111) and Au(211). Increased stability is associated with a more negative energy. As seen in Table S4, the differences in energy between paired Cu atoms and maximally separate Cu atoms are negligible. Therefore, we conclude there is no preference for Cu clusters (and Cu_2 ensembles), but they form randomly following the overall availability of Cu atoms on the surface.

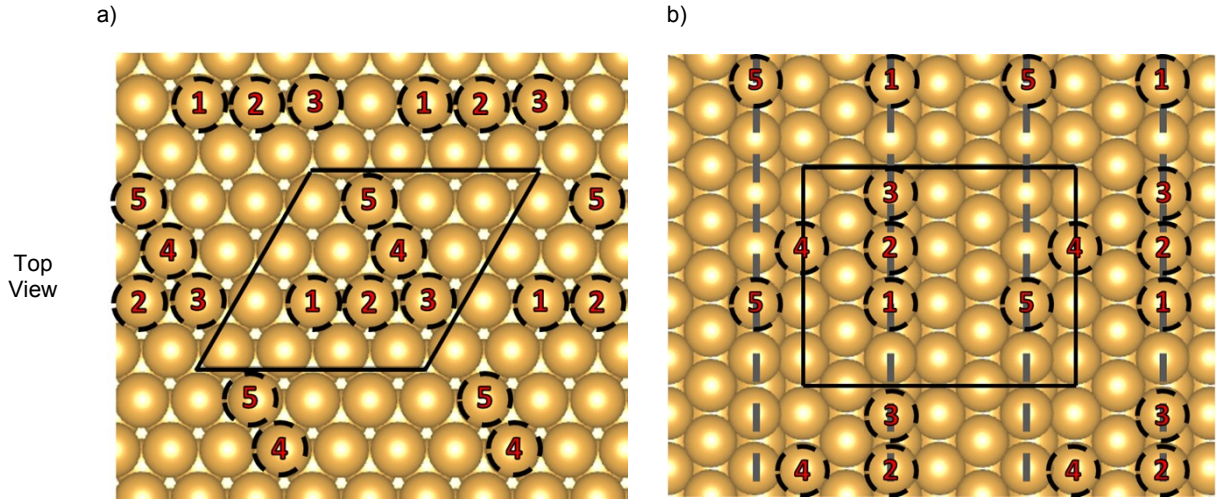

Figure S9. Illustration of top views of (a) Au(111), (b) Au(211). The black boxes, dashed lines and the labeled sites are periodic boundaries, stepedge and Cu surface dopants sites, respectively.

Table S4: Cu dopant cluster stability results

	ΔE_{DFT} (eV)	
Slab	Au(111)	Au(211)
Case 1	0	0
Case 2	−0.02	−0.02
Case 3	−0.01	0.05
Case 4	−0.02	0.02

S9. Alternative bimetallic slab models

In the manuscript we have used a bulk Au(211) slab with surface Cu dopants to represent the Cu/Au bimetallic (BM) nanoparticles. This is an approximation where we have assumed near surface layers are dominated by Au. However, we have explored more realistic slab models that incorporate Cu with the sublayers of the slab which would be closer to the experimental Cu/Au bimetallic nanoparticles. All bimetallic surface slab models use the (211) surface orientation. We assumed that each bimetallic surface slab model has a laterally compressed lattice parameter depending on the ratio of Au and Cu. Figure S10(a) shows the pure Au(211) slab (used in the manuscript). Figure S10(b) is a slab with the bottom layer composed of Cu atoms and the top 3 layers composed of Au atoms. Fig. S10(c) is a slab where the bottom layer is composed of Cu atoms and the top layer of Au atoms, but the 2 intermediate layers are composed of a mixture of Au/Cu atoms with a ratio of 3:1.

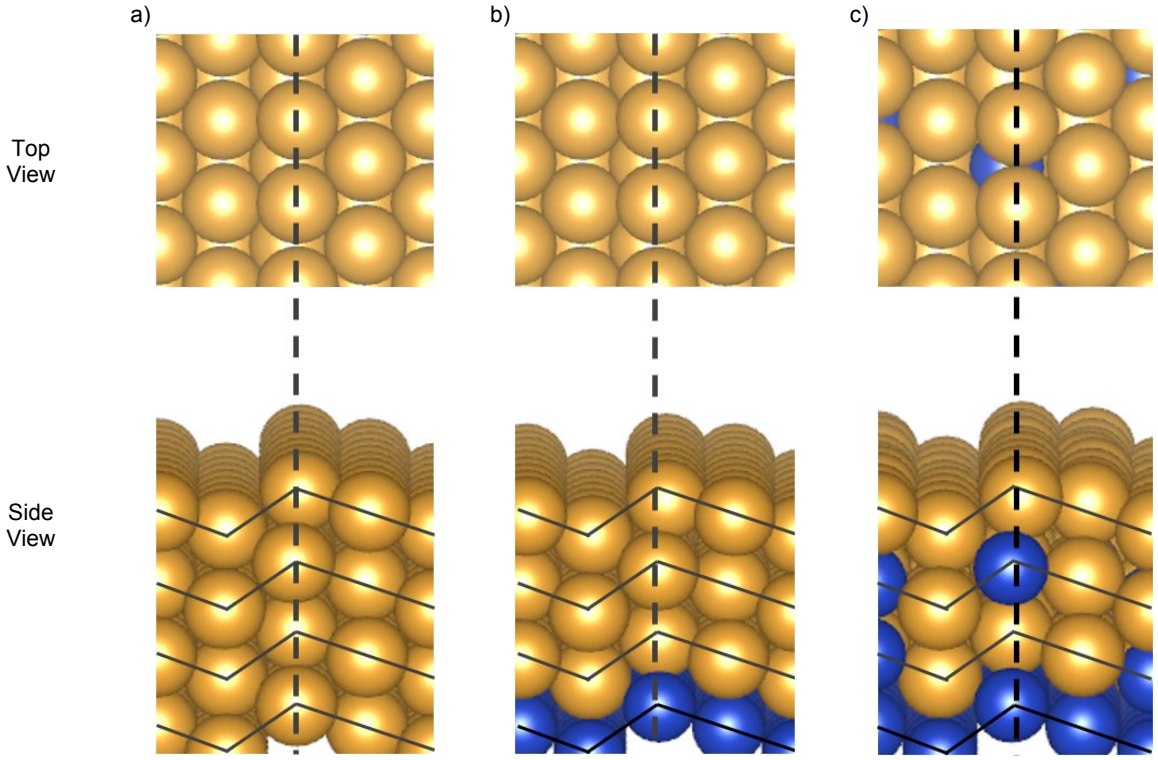

Figure S10. Illustration of top and side views of (a) Au(211), (b) 3Au-1Cu and (c) Au-2BM-Cu. The dashed and solid lines illustrate the positions of a step edge and a layer, respectively. Yellow and blue atoms are Au and Cu, respectively.

In the manuscript, we show the free energy of adsorption with Cu surface dopants on pure Au(211). We also explored and compared these results with the bimetallic surface slabs shown in Figure S10 (3Au-1Cu & 1Au-2BM-1Cu) and pure Au(211). The ΔG for COOH*, CHOO*, and H* as a function of Cu dopants for all three models are illustrated in Figure S11. The values are tabulated in Table S4 further below. Even though the free energies are not identical with each other, the trend for the relative free energies amongst COOH*, CHOO* and H* are similar. In particular, the introduction of Cu dopants stabilizes both COOH* and CHOO* for a single Cu atom dopant, but the addition of 2 Cu atom dopants stabilizes the CHOO* far more dramatically than COOH*. Similarly, the ΔG for H* is positive until 3 Cu dopants are introduced where there is a drop to values similar to pure Cu(211). Overall, these results demonstrate that while there are differences based on the slab model for the bimetallic surface, the key ensemble effect of a Cu_2 local site that favors CHOO* formation over COOH* while retaining the positive ΔG for H* observed for Au(211) is common to all the slabs.

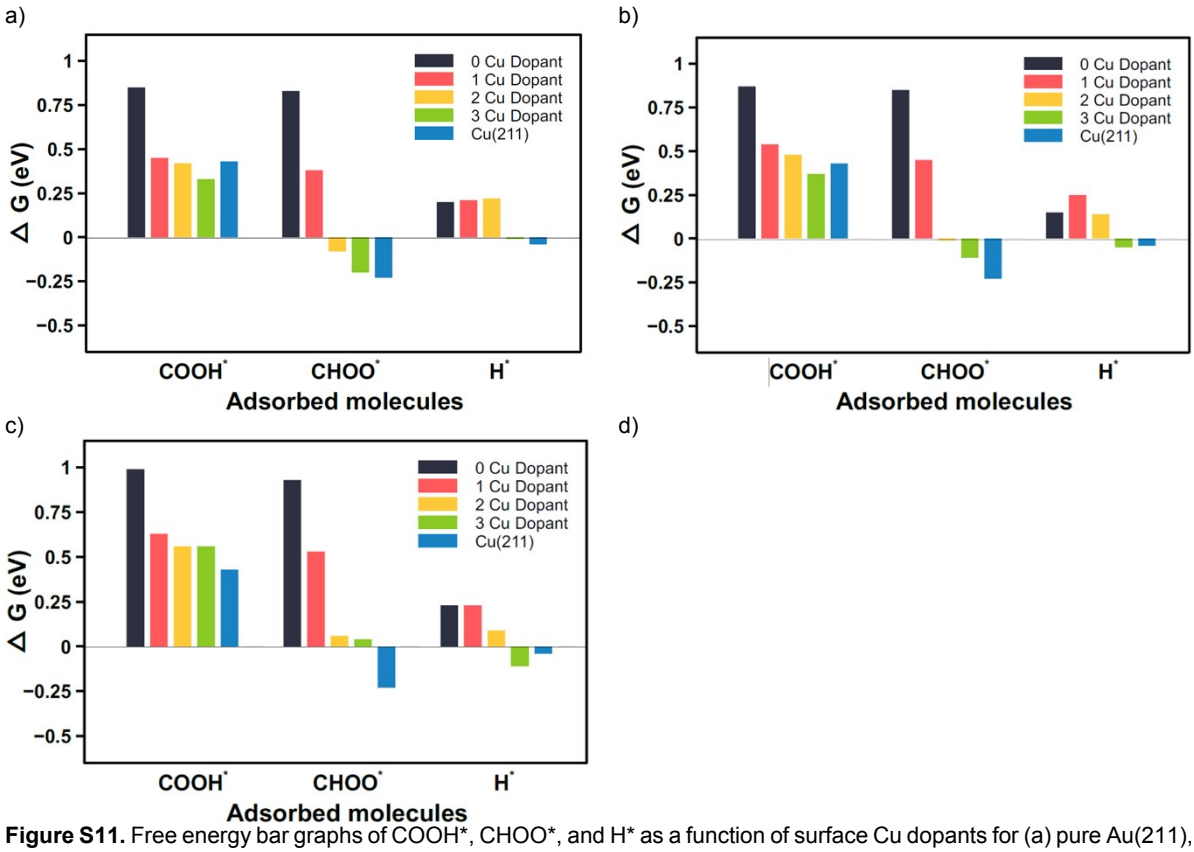

Figure S11. Free energy bar graphs of COOH*, CHOO*, and H* as a function of surface Cu dopants for (a) pure Au(211), (b) 3Au-1Cu and (c) 1Au-2BM-1Cu slab models.

Table S5: △G of adsorbates on various bimetallic slabs as a function of surface Cu dopants.

# Surface Dopants	Slab information	△G(eV)		
		COOH*	CHOO*	H*
0Cu	Pure Au(211)	0.85	0.83	0.20
	3Au-1Cu	0.87	0.85	0.15
	Au-2BM-Cu	0.99	0.93	0.23
1Cu	Au(211)	0.45(Cu-O bond)	0.38	0.21
	3Au-1Cu	0.54(Cu-O bond)	0.45	0.25
	Au-2BM-Cu	0.63(Cu-O bond)	0.53	0.23
2Cu	Au(211)	0.42	-0.08	0.22
	3Au-1Cu	0.48	-0.00	0.14
	Au-2BM-Cu	0.56	0.06	0.09
3Cu	Au(211)	0.33	-0.20	-0.01
	3Au-1Cu	0.37	-0.11	-0.05
	Au-2BM-Cu	0.56	0.04	-0.11
N/A	Pure Cu(211)	0.43	-0.23	-0.04

S10. Configurations of adsorbates on Au(211) slab

In Figure S12, we show relaxed adsorbate images on surface with 3 Cu dopant atoms. The favored orientation and adsorption site of the CHOO*, COOH*, and H* are the same as a function of Cu dopants, but as shown in Figure 3(e) in the manuscript the O-metal bonding is stronger with Cu atoms versus Au atoms.

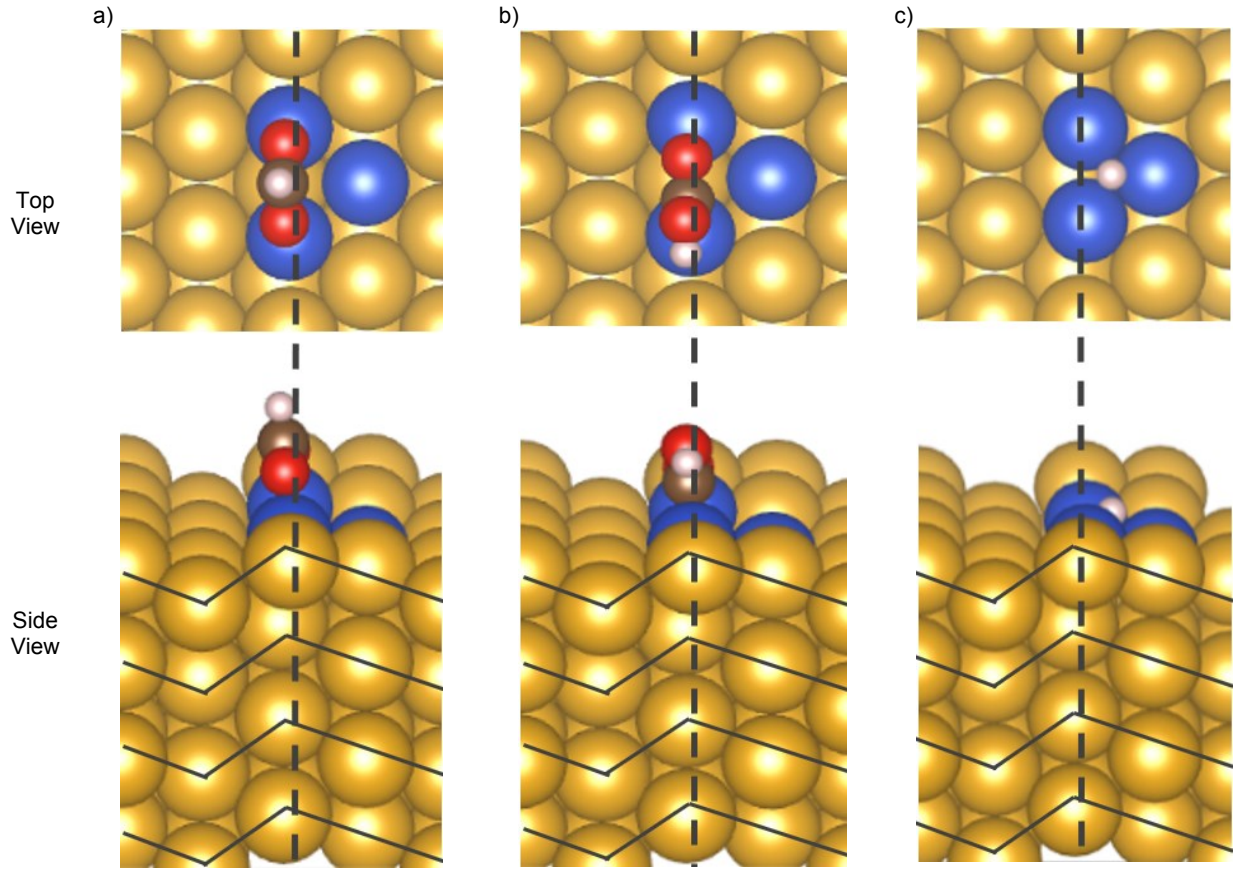

Figure S12. Illustration of the top and side views of Au(211) relaxed images with adsorbates (CHOO*, COOH* and H* in order) on 3 Cu surface dopants. Yellow, blue, red, dark brown and white atoms are Au, Cu, oxygen, carbon and hydrogen, respectively.

S11. DFT calculations on low-Miller index facets of Au

We have used DFT to evaluate the free energy for COOH*, CHOO*, and H* formation on the low-Miller index facets of Au. All DFT details are equivalent with the Au(211) calculations reported in the paper. Fig. S13 shows the ΔG results of HER, COOH* and CHOO* pathways on (211), (111), (110), and (100) surfaces. Even though the absolute ΔG values are different from each surface domain, the relative difference of HER, HCOO and COOH in each domain shows similar trends over all surfaces that the small amounts of Cu increased the selectivity of formate. Figure S14 a and b show the $\Delta\Delta G$(COOH*-CHOO*) and ΔG of the Hydrogen Evolution Reaction (HER) to more clearly see the effect of copper addition.

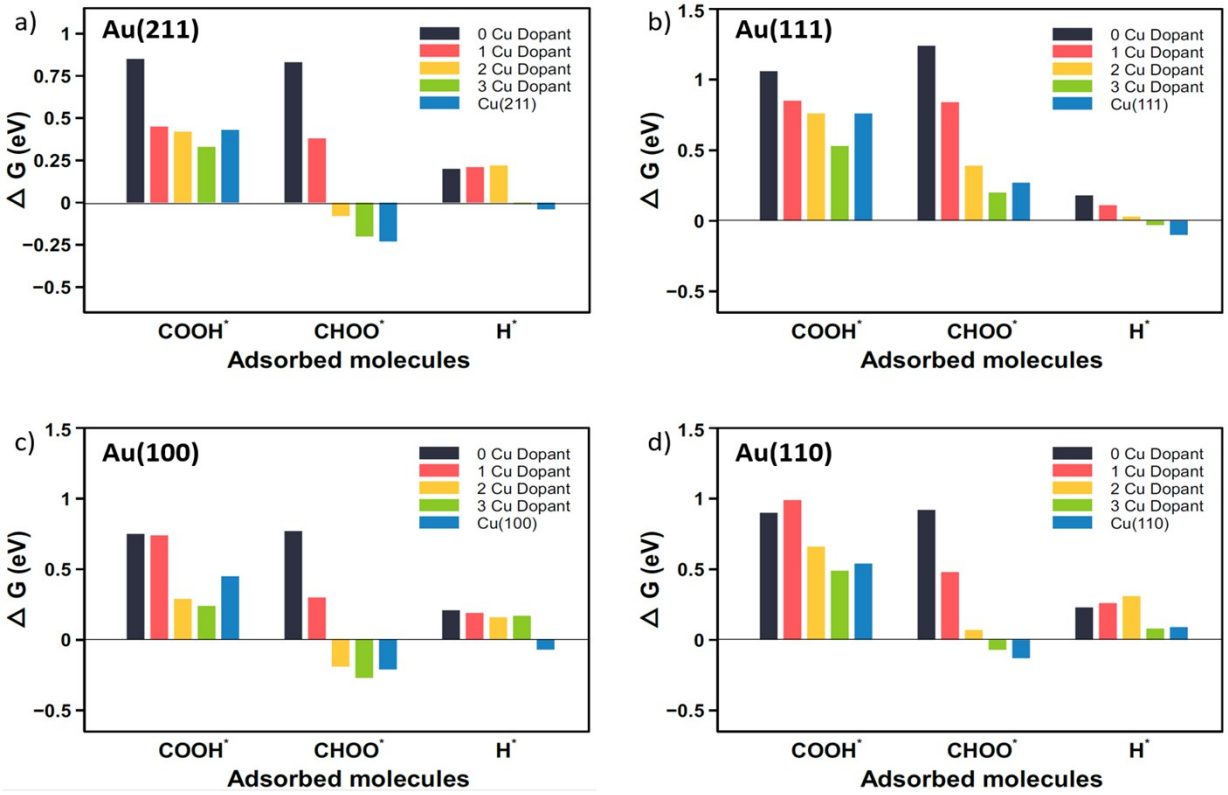

Figure S13. Free energy bar graphs of COOH*, CHOO*, and H* as a function of surface Cu dopants for (a) pure Au(211), (b) pure Au(111) (c) pure Au(100), and (d) pure Au(110).

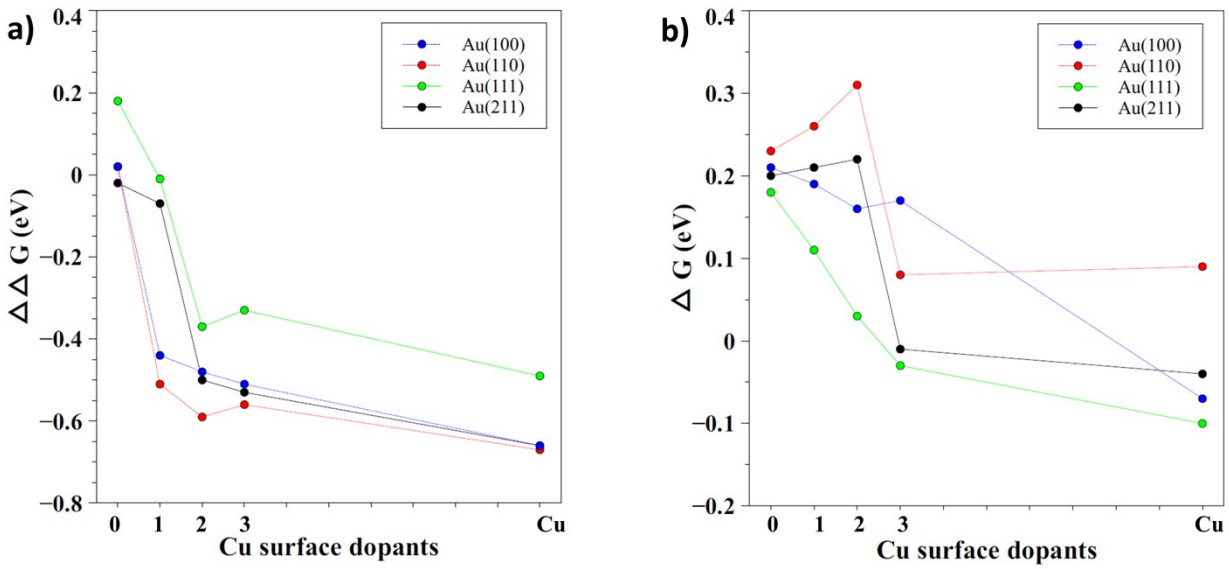

Figure S14. Free energy plots as a function of surface Cu dopants for (a) $^{\Delta\Delta}$G(COOH*-CHOO*) and (b) $^{\Delta}$G (HER) on Au(100), Au(110), pure Au(111), and Au(211).

Table S6: △G of adsorbates on various bimetallic slabs as a function of surface Cu dopants.

slab information	# surface Cu dopants	△G (eV)		
		COOH*	CHOO*	H*
Au(100)	0	0.75	0.77	0.21
Au(100)	1	0.74	0.3	0.19
Au(100)	2	0.29	-0.19	0.16
Au(100)	3	0.24	-0.27	0.17
Cu(100)		0.45	-0.21	-0.07
Au(110)	0	0.9	0.92	0.23
Au(110)	1	0.99	0.48	0.26
Au(110)	2	0.66	0.07	0.31
Au(110)	3	0.49	-0.07	0.08
Cu(110)		0.54	-0.13	0.09
Au(111)	0	1.06	1.24	0.18
Au(111)	1	0.85	0.84	0.11
Au(111)	2	0.76	0.39	0.03
Au(111)	3	0.53	0.2	-0.03
Cu(111)		0.76	0.27	-0.1
Au(211)	0	0.85	0.83	0.2
Au(211)	1	0.45	0.38	0.21
Au(211)	2	0.42	-0.08	0.22
Au(211)	3	0.33	-0.2	-0.01
Cu(211)		0.43	-0.23	-0.04

Reference

1. Hofmann, D. M., Fairbrother, D. H., Hamers, R. J. & Murphy, C. J. Two-Phase Synthesis of Gold–Copper Bimetallic Nanoparticles of Tunable Composition: Toward Optimized Catalytic CO2 Reduction. *ACS Appl. Nano Mater.* **2**, 3989–3998 (2019).

2. Zhang, B. A., Ozel, T., Elias, J. S., Costentin, C. & Nocera, D. G. Interplay of Homogeneous Reactions, Mass Transport, and Kinetics in Determining Selectivity of the Reduction of CO2 on Gold Electrodes. *ACS Cent. Sci.* **5**, 1097–1105 (2019).

3. Chen, Y., Li, C. W. & Kanan, M. W. Aqueous CO2 reduction at very low overpotential on oxide-derived au nanoparticles. *J. Am. Chem. Soc.* **134**, 19969–19972 (2012).

4. Harvey, D. *Modern analytical chemistry*. vol. 1 (McGraw-Hill New York, 2000).

5. Konopka, S. J. & McDuffie, B. Diffusion coefficients of ferri-and ferrocyanide ions in aqueous media, using twin-electrode thin-layer electrochemistry. *Anal. Chem.* **42**, 1741–1746 (1970).

6. Cheng, G. & Walker, A. R. H. Transmission electron microscopy characterization of colloidal copper nanoparticles and their chemical reactivity. *Anal. Bioanal. Chem.* **396**, 1057–1069 (2010).

7. Mezzavilla, S., Horch, S., Stephens, I. E. L., Seger, B. & Chorkendorff, I. Structure sensitivity in the electrocatalytic reduction of CO2 with Gold catalysts. *Angew. Chemie Int. Ed.* **58**, 3774–3778 (2019).

8. Zhu, W. *et al.* Monodisperse Au nanoparticles for selective electrocatalytic reduction of CO2 to CO. *J. Am. Chem. Soc.* **135**, 16833–16836 (2013).

9. Back, S., Yeom, M. S. & Jung, Y. Active sites of Au and Ag nanoparticle catalysts for CO2 electroreduction to CO. *Acs Catal.* **5**, 5089–5096 (2015).

10. Hahn, C. *et al.* Engineering Cu surfaces for the electrocatalytic conversion of CO2: Controlling selectivity toward oxygenates and hydrocarbons. *Proc. Natl. Acad. Sci.* **114**, 5918–5923 (2017).

11. Vickers, J. W., Alfonso, D. & Kauffman, D. R. Electrochemical carbon dioxide reduction at nanostructured gold, copper, and alloy materials. *Energy Technol.* **5**, 775–795 (2017).

12. Krylova, V. & Andrulevičius, M. Optical, XPS and XRD studies of semiconducting copper sulfide layers on a polyamide film. *Int. J. Photoenergy* **2009**, (2009).

13. Shinagawa, T., Larrazábal, G. O., Martín, A. J., Krumeich, F. & Pérez-Ramírez, J. Sulfur-modified copper catalysts for the electrochemical reduction of carbon dioxide to formate. *ACS Catal.* **8**, 837–844 (2018).

14. Li, G. *et al.* Three-dimensional porous carbon composites containing high sulfur nanoparticle content for high-performance lithium–sulfur batteries. *Nat. Commun.* **7**, 1–10 (2016).

15. Shang, H. *et al.* Effect of surface ligands on gold nanocatalysts for CO2reduction. *Chem. Sci.* **11**, 12298–12306 (2020).

16. Blöchl, P. E. Projector augmented-wave method. *Phys. Rev. B* **50**, 17953 (1994).

17. Kresse, G. Ab initio molecular dynamics for liquid metals. *J. Non. Cryst. Solids* **192**, 222–229 (1995).

18. Kresse, G. & Hafner, J. Ab initio molecular dynamics for liquid metals. *Phys. Rev. B* **47**, 558 (1993).

19. Perdew, J. P., Burke, K. & Ernzerhof, M. Generalized gradient approximation made simple. *Phys. Rev. Lett.* **77**, 3865 (1996).

20. Nørskov, J. K. *et al.* Origin of the overpotential for oxygen reduction at a fuel-cell cathode. *J. Phys. Chem. B* **108**, 17886–17892 (2004).

21. Peterson, A. A., Abild-Pedersen, F., Studt, F., Rossmeisl, J. & Nørskov, J. K. How copper catalyzes the electroreduction of carbon dioxide into hydrocarbon fuels. *Energy Environ. Sci.* **3**, 1311–1315 (2010).